A study of infrasound propagation based on high-order finite difference solutions of the Navier-Stokes equations

O. Marsden,[a] C. Bogey, and C. Bailly
Laboratoire de Mécanique des Fluides et d'Acoustique, UMR CNRS 5509, Ecole Centrale de Lyon, Université de Lyon, 69134 Ecully cedex, France

(Received 30 September 2013; revised 14 January 2014; accepted 28 January 2014)

The feasibility of using numerical simulation of fluid dynamics equations for the detailed description of long-range infrasound propagation in the atmosphere is investigated. The two dimensional (2D) Navier Stokes equations are solved via high fidelity spatial finite differences and Runge-Kutta time integration, coupled with a shock-capturing filter procedure allowing large amplitudes to be studied. The accuracy of acoustic prediction over long distances with this approach is first assessed in the linear regime thanks to two test cases featuring an acoustic source placed above a reflective ground in a homogeneous and weakly inhomogeneous medium, solved for a range of grid resolutions. An atmospheric model which can account for realistic features affecting acoustic propagation is then described. A 2D study of the effect of source amplitude on signals recorded at ground level at varying distances from the source is carried out. Modifications both in terms of waveforms and arrival times are described.
© *2014 Acoustical Society of America*. [http://dx.doi.org/10.1121/1.4864793]

PACS number(s): 43.28.Dm, 43.28.Js, 43.28.Fp [RMW] Pages: 1083–1095

I. INTRODUCTION

It has been known since the early modern period and the rapid development of cannons in warfare that low frequency sounds produced on battle fields can be heard at great distance, and also that sound amplitude is a non-monotonous function of distance from the source. A detailed history of such observations as well as the chronology of work aiming to explain propagation phenomena can be found in the review article by Delany.[1]

Although most of the theory regarding long-distance acoustic propagation in the atmosphere is now agreed upon, the prediction of the time signature of a given source at a given distance remains a complicated task, due to the variety of phenomena which affect propagation. A brief, non-exhaustive list includes convection due to wind, refraction due to both temperature and wind speed gradients, scattering on smaller scale meteorological inhomogeneities, non-linear waveform distortion, caustics, atmospheric absorption, ground and terrain effects.[2–5] Simplified modeling approaches easily amenable to propagation over long distances are not able to account for all of these physical effects. This is the case for approaches based on the fast field program (FPP) and parabolic equations (PE), which have been used extensively to study acoustic propagation.[6–8] Such approaches provide approximate solutions to the wave equation, and suffer from limitations due both to the resolution technique, e.g., FFP is limited to horizontally homogeneous problems while PE methods have angular limitations, and to the wave equation itself, in particular its linearity. It should be noted that recently developed non-linear parabolic equations[9] alleviate the latter problem. Ray tracing, based on the geometrical acoustics approximation, has also been widely employed for propagation problems since the early work of Blokhintsev.[10,11] State of the art ray tracing developments allow finite amplitude signals to be modeled along ray trajectories.[12] However ray tracing does not in itself predict scattering and diffraction due to atmospheric inhomogeneities and caustics, both of which can have a significant impact on pressure signals received far from the source.[13,14] Recently, efforts have been made toward long-range propagation studies based directly on the full Navier-Stokes equations,[15–17] or on a set of linearized fluid dynamic equations.[18–20] The full set of equations should allow a correct description of the whole gamut of propagation effects mentioned previously, but the resolution of these equations in a computationally affordable way requires the use of well suited numerical techniques. Accurate predictions of long distance propagation in realistic conditions is of use to a range of fields, including international military monitoring[21] and atmospheric studies.[22]

In this work, the full two-dimensional Navier-Stokes equations are solved to model the propagation of low-frequency sound waves through the atmosphere. The atmosphere is modeled from ground level to an altitude of 160 km. It is stratified due to gravity, and has a mean temperature profile which mimics the large-scale variations observed in experimental profiles.[14,23] Explicit finite differences based on 11-point stencils are used to compute the spatial derivatives involved in the Navier-Stokes equations. Time integration is performed with a six-stage optimized Runge-Kutta scheme. Additionally, a shock-capturing filtering technique is employed in order to handle the discontinuities that appear in the vicinity of shock waves. The full numerical algorithm has been implemented in a functionally equivalent manner in FORTRAN 90 and in OpenCL allowing performance to be ascertained on a variety of hardware. Benchmark problems in both homogenous and inhomogeneous atmospheric conditions are used to ascertain the effect of grid resolution on

[a]Author to whom correspondence should be addressed. Electronic mail: olivier.marsden@ec-lyon.fr

Redistribution subject to ASA license or copyright; see http://acousticalsociety.org/content/terms. Download to IP: 156.18.39.37 On: Fri, 07 Mar 2014 09:48:20

long range acoustic predictions. The effect of source amplitude on long-distance 2D propagated time signals is examined.

The paper is organized as follows. After a general introduction, the set of equations and numerical algorithm are described in Sec. II. Section III is devoted to an examination of the algorithm's fidelity as a function of grid resolution, for two propagation test problems. In Sec. IV a description of time signals resulting from long range propagation is given, along with a study of the modifications of time signatures due to variations in source amplitude.

II. NUMERICAL ALGORITHM

Propagation over long distances of large-amplitude sounds is not correctly described by a linear model, as will be illustrated later in this paper. Therefore, fluid motion is modeled in this work in two dimensions with the standard non-linearized fluid dynamics equations, namely that of mass conservation, the Navier-Stokes equation and an energy equation, completed by the perfect gas law. In Cartesian coordinates, this set of equations governing the flow variables $\mathbf{U} = (\rho,\ \rho u_1,\ \rho u_2,\ \rho e_t)^T$, where e_t is the specific total energy given for a perfect gas by $\rho e_t = p/(\gamma - 1) + 1/2\,\rho u_i^2$, can be written as

$$\frac{\partial \mathbf{U}}{\partial t} + \frac{\partial \mathbf{E_1}}{\partial x_1} + \frac{\partial \mathbf{E_2}}{\partial x_2} - \frac{\partial \mathbf{V_1}}{\partial x_1} - \frac{\partial \mathbf{V_2}}{\partial x_2} + \frac{\partial \mathbf{Q_1}}{\partial x_1} + \frac{\partial \mathbf{Q_2}}{\partial x_2} + \mathbf{C} = 0, \tag{1}$$

where the Eulerian, viscous and thermal fluxes are defined by

$$\begin{aligned}
&\mathbf{E_1} = [\rho u_1,\ p + \rho u_1^2,\ \rho u_1 u_2,\ (\rho e_t + p)u_1]^T,\\
&\mathbf{E_2} = [\rho u_2,\ \rho u_1 u_2,\ p + \rho u_2^2,\ (\rho e_t + p)u_2]^T,\\
&\mathbf{V_1} = (0,\ \tau_{11},\ \tau_{12},\ u_1\tau_{11} + u_2\tau_{12})^T,\\
&\mathbf{V_2} = (0,\ \tau_{21},\ \tau_{22},\ u_1\tau_{21} + u_2\tau_{22})^T,\\
&\mathbf{Q_i} = [0,\ 0,\ 0,\ -(\mu c_p/\sigma)\partial T/\partial x_i]^T,\\
&\text{with}\quad \tau_{ij} = \mu(\partial u_i/\partial x_j + \partial u_j/\partial x_i - 2/3\delta_{ij}\partial u_k/\partial x_k),\\
&\text{and}\quad \mathbf{C} = (0,\ 0,\ \rho g,\ \rho g u_2)^T,
\end{aligned} \tag{2}$$

where μ is the dynamic viscosity coefficient, σ is the Prandtl number of the fluid, c_p is the specific heat at constant pressure, and γ is the fluid's equilibrium specific heat ratio.

The previous set of Eqs. (1) and (2) does not describe molecular relaxation effects, which contribute to acoustic absorption and dispersion during propagation. Although the set of equations can be modified to account for these dissipative and dispersive effects,[17,24] they have been shown to be small when compared to other phenomena involved in long-range propagation.[24] Accordingly, these effects are not modeled in this work. This simplification avoids the need to track the individual gaseous components of the atmosphere, allowing the mixture to be modeled as an equivalent perfect gas.

Mean properties of the atmosphere are very strongly altitude-dependent, due in large part to the gravity-driven density stratification, and to the temperature profile. Indeed, over the altitude range relevant to long-distance propagation, from 0 to around 160 km, both average pressure and average density diminish by a factor of almost 10 orders of magnitude. This poses significant numerical difficulties, for example simply to ensure stability of the mean profiles,[25] which stems from the hydrostatic equilibrium condition $d\bar{p}/dx_2 = -\bar{\rho}g$ whose finite difference approximation must be verified numerically to a high degree of accuracy. Rewriting Eq. (1) as

$$\frac{\partial \mathbf{U}}{\partial t} + \frac{\partial \mathbf{E_1}}{\partial x_1} + \frac{\partial \mathbf{E_2'}}{\partial x_2} - \frac{\partial \mathbf{V_1}}{\partial x_1} - \frac{\partial \mathbf{V_2}}{\partial x_2} + \frac{\partial \mathbf{Q_1}}{\partial x_1} + \frac{\partial \mathbf{Q_2}}{\partial x_2} + \mathbf{C'} = 0, \tag{3}$$

with $\mathbf{C'} = [0,\ 0,\ (\rho - \bar{\rho})g,\ (\rho - \bar{\rho})gu_2 + \bar{p}\partial u_2/\partial x_2]^T$ and $\mathbf{E_2'} = \{\rho u_2,\ \rho u_1 u_2,\ (p - \bar{p}) + \rho u_2^2,\ [\rho e_t + (p - \bar{p})]u_2\}^T$ is mathematically equivalent as long as mean fields are invariant in the x_1 direction, but numerically far more favorable because the aforementioned average hydrostatic stability condition is not computed numerically at each time step. These equations are solved on a regular Cartesian grid with an optimized high-fidelity numerical procedure based on explicit spatial finite differences and Runge-Kutta time integration. Where possible, spatial discretization is performed with explicit fourth-order 11-point centered finite differences optimized to minimize dispersion for wavenumbers discretized by between four and 32 grid points.[26] Close to boundaries, be they the ground or radiation conditions, optimized explicit non-centered differencing schemes are used.[27] The non-centered differencing schemes are all based on 11-point stencils, including the one-sided stencil used for wall points. Time integration is performed with a six-step second-order optimized low-storage Runge-Kutta algorithm.[26] Characteristics regarding dispersion and dissipation for the spatial differencing schemes and the time integration scheme can be found in previous papers.[26,27] The schemes' properties mean that the behavior of waves discretized by at least four points per wavelength is accurately reproduced, with very low levels of dispersion and dissipation, and is stable up to frequencies such that $\omega\Delta t \leq 1.25 \times \pi$. The determination of the computational time step Δt is based on a CFL (Courant-Friedrichs-Lewy) condition, $\mathrm{CFL} = c_{\max}\Delta t/\Delta x_{\min}$, where $c_{\max}$ is the largest value of the speed of sound in the atmosphere modeled here, and $\Delta x_{\min}$ the smallest grid spacing in the mesh. A value of $\mathrm{CFL} = 0.5$ is used throughout this work. The ground is modeled as a non-slip boundary condition, except for the inviscid validation test cases, where the ground is modeled with a slip condition. The wall-point flow variables are updated by solving the governing equations with the aforementioned high-order non-centered differencing schemes.

Spatial low-pass filtering is carried out to ensure stable computations. An explicit sixth-order 11-point filtering stencil is designed to remove fluctuations discretized by less than four grid points per wavelength, while leaving larger wavelengths effectively untouched.[28] As the differencing schemes used near boundaries are asymmetric, their effective wavenumbers have an imaginary part which leads to them being unstable for very high frequencies.[29] It is therefore, essential to use them in conjunction with appropriate highly selective filters, and to this end, the filters described

Redistribution subject to ASA license or copyright; see http://acousticalsociety.org/content/terms. Download to IP: 156.18.39.37 On: Fri, 07 Mar 2014 09:48:20

in Berland *et al.*,[27] which also selectively damp fluctuations with fewer than four points per wavelength have been implemented. Filters for grid points more than two points away from a boundary are built on 11-point stencils, while stencils for the wall point and for the first point away from the wall are built on four and seven points, respectively. Thus at the ground, in the x_1 direction, the centered 11-point filter is used, whereas in the x_2 direction the family of non-centered filters is applied.

At the lateral radiation boundaries in the x_1 and x_2 directions, Tam and Webb's 2D far-field radiation condition[30] is applied. The left and right radiation conditions are supplemented by sponge zones combining grid stretching and low-order spatial filtering, a technique commonly used in computational aeroacoustics.[31] A simple radiation boundary condition along the top boundary generates unsatisfactorily large reflected waves, which contaminate pressure signals at ground level. Unfortunately, stratification of the atmosphere due to gravity renders the top boundary less amenable than the side boundaries to a standard sponge layer approach. Indeed, for a given source strength the ratio of generated pressure fluctuations to ambient pressure increases with altitude,[32] and is proportional to $(1/r)\sqrt{\gamma/(\bar{c}^2\bar{p})}$ in 3D, and $(1/\sqrt{r})\sqrt{\gamma/(\bar{c}^2\bar{p})}$ in 2D as in the present work, where r is the propagation distance since the source. This means that extending the computational domain vertically with a sponge zone will also increase the relative amplitude of the fluctuations needing to be evacuated through the boundary condition. The radiation condition being based on the linearized Euler equations,[30] the amplitude of spurious reflected waves generated by the boundary condition will increase linearly with the amplitude of physical outgoing waves. Thus, at ground level, the spurious reflected wave amplitude does not decrease as could be expected when a simple sponge zone is applied. Instead, in this work, the useful computational domain is extended vertically with a sponge zone in which the gravity profile varies progressively from its expected value $g(x_2)$ to $-g(x_2)$ following a $\tanh(x_2/h)$ variation where h is set to three wavelengths of the main source frequency at the altitude in question. Once negative gravity has been reached, the ratio of pressure fluctuations to ambient pressure no longer increases but decreases, allowing standard grid stretching techniques and low-order dissipation to operate as in a typical sponge zone used in the computational aeroacoustics community. This approach allowed spurious reflections to be reduced to background error levels.

Non-linear effects can be important in long-range atmospheric propagation, due both to the sizable propagation distances and to large relative amplitudes which are reached in the high atmosphere. For strong amplitude sources, acoustic shocks are rapidly formed close to the source. It is also surmised that shock fronts may be formed in the thermosphere, regardless of the source amplitude. This aspect poses potential problems for standard finite-difference time-domain acoustic solvers, which are not designed to cope with steep wave fronts and which can lead to unacceptably large Gibbs oscillations and divergent computations. The computational fluid dynamics (CFD) community has been dealing with shocked flows for a long time, and has developed a variety of different techniques to avoid numerical problems associated with the presence of shocks. Standard shock-capturing schemes developed for CFD are however ill-suited to time-dependent problems, because they exhibit poor spectral accuracy,[33] and tend to be excessively dissipative, particularly in the context of long-distance propagation. Hence in this work we employ a non-linear filtering method designed with acoustics and aeroacoustics in mind.[28] The methodology consists in applying a second-order conservative filter only where necessary, i.e., only in the vicinity of shock fronts. Understandably, much of the method's properties come from the non-linear detection algorithm. Non-linear zones are identified thanks to a Jameson-like detector based on pressure fluctuations. The first step consists in extracting the high wavenumber components from pressure fluctuations. This is done by applying a second-order filtering, as described in the following equation for grid point i, in the x_1 direction:

$$Dp_i = (-p_{i+1} + 2p_i - p_{i-1})/4 \tag{4}$$

and then defining the high-pass filtered squared pressure fluctuation as

$$D_i^2 = \frac{1}{2}[(Dp_i - Dp_{i-1})^2 + (Dp_i - Dp_{i+1})^2]. \tag{5}$$

This squared pressure fluctuation is used to define a sensor value as

$$r_i = \frac{D_i^2}{\overline{p_i}^2} + \epsilon, \tag{6}$$

where ϵ is a small parameter, typically 10^{-16}, whose role is to avoid numerical problems when dividing by r_i, as will be seen subsequently, and is the averaged pressure at point i. The self-adjusting filtering strength σ_i at grid point i is computed according to

$$\sigma_i = \frac{1}{2}\left(1 - \frac{r_{\text{th}}}{r_i} + \left|1 - \frac{r_{\text{th}}}{r_i}\right|\right), \tag{7}$$

where r_{th} is a threshold constant whose value is $r_{\text{th}} = 10^{-5}$. This filtering strength has the desired properties of being equal to zero away from shocks, where $r_i < r_{\text{th}}$, and of increasing toward a value of 1 for increasing shock intensities. Conservative variables are filtered conservatively, i.e., the filtered term is computed as a difference of two fluxes, as follows:

$$U_i^f = U_i - \alpha\left(\sigma_{i+1/2}F_{i+1/2} - \sigma_{i-1/2}F_{i-1/2}\right), \tag{8}$$

where $\sigma_{i+1/2}$ is simply the average of previously calculated filtering strengths σ_i and σ_{i+1}, and $F_{i+1/2} = \sum_{j=1-n}^{n} c_j U_{i+j}$ and $F_{i-1/2} = \sum_{j=1-n}^{n} c_j U_{i+j-1}$ are the up-winded and down-winded fluxes based on a dissipative second-order filter c_j. The amplitude α is there to allow a fine adjustment of the total filtering magnitude, as will be seen subsequently. It is, in general, set to $\alpha = 1$. A spectral analysis of the shock-capturing

Redistribution subject to ASA license or copyright; see http://acousticalsociety.org/content/terms. Download to IP: 156.18.39.37 On: Fri, 07 Mar 2014 09:48:20

treatment is in Bogey *et al.*,[28] and an example of the scheme's behavior for an acoustic signal typical of long range propagation scenarios is provided in Sec. IV C 1.

Examples of 2D acoustic diffraction and aeroacoustic flows successfully simulated with the solver described in this work can be found in Marsden *et al.*[34] and Berland *et al.*[27] The same methodology has been applied to numerous aeroacoustic studies in 3D,[35–38] and the generalization of the currently described solver to three dimensions should pose no difficulties other than that of the computational cost of the resulting 3D computations.

Finally, the entire code has been ported from FORTRAN 90 parallelized with OpenMP, to OpenCL, maintaining the code functionally identical. This has allowed performance to be tested on a variety of hardware, both CPU (Central Processing Unit) and GPU (Graphics Processing Unit). Results from this non-exhaustive testing are summarized in Table I. The baseline is taken as the execution speed of the optimized Fortran code on a problem of size 5 M points in which IO has been removed, compiled with the Intel Fortran compiler and run on a single Intel X5550 processor core (2.67 GHz). The same code, run in shared memory OpenMP mode on four cores, performs almost three times faster, providing reasonable strong scaling. Intel has relatively recently published an OpenCL toolkit allowing code to be run on their CPUs. The OpenCL code running on four cores slightly outperforms the OpenMP F90 version. Performance on the GPUs is vastly better. On a previous generation NVIDIA card destined to the HPC market, performance is 26 times higher than on a single CPU core, while on the current generation general public card from AMD, performance is an impressive 57 times higher. This GPU performance, combined with the CPU performance obtained with essentially the same code base, highlights the versatility and power of OpenCL as a cross-platform computing language. It should be noted that although very good performance is possible over a wide range of hardware, this performance is not obtained automatically. Code tuning for each architecture was found to be highly beneficial in this work, in particular to take into account large architectural differences between CPU and GPU, but also to accommodate for smaller differences between GPUs, such as the size of local memory.

III. APPLICATION TO BENCHMARK PROBLEMS

The solver is applied to two test cases in order to study grid requirements for the correct representation of important physical phenomena relevant to long-distance atmospheric propagation.

TABLE I. Normalized code performance, on one (1C) or four (4C) Intel X5550 CPU cores and on two different GPUs, for a 5 million point simulation.

Intel X5550 (1C)	X5550 (4C)	X5550 (4C)	NVIDIA M2050	AMD HD7970
F90	F90-OpenMP	OpenCL	OpenCL	OpenCL
1	2.8	3.2	26	57

A. Acoustic source in a homogeneous atmosphere

The first problem is the inviscid linear prediction of the acoustic field resulting from a harmonic monopole source located near a flat rigid surface in a homogeneous atmosphere. The analytical solution to this problem was published by Morse and Ingard,[39] and results simply from the sum of the monopole's direct radiated field and of the field radiated by the monopole's image with respect to the wall. For the present study, a monopolar source at a frequency of 100 Hz is placed at a height of 20 m above a wall, as in the work of Wilson and Liu[40] and Ostashev *et al.*[18] The source shape is given by a Gaussian of half-width 0.8 m. Ambient pressure is set to 10^5 Pa, and ambient density such that speed of sound is equal to $c_0 = 340$ m/s. In order to ensure negligible nonlinear steepening, the monopolar source amplitude is set to a very low value of 10^{-2} Pa. Numerical solutions are compared to the analytical solution along a line parallel to the ground at the source altitude of 20 m, over a distance of 100 m. They are compared in terms of transmission loss, $\mathrm{TL}(x) = 20\log_{10}[p(x)/p_{\mathrm{ref}}]$ where p_{ref} is the pressure amplitude at 1 m from the same monopole in a free field, and of error, defined here according to $\epsilon = (1/99)\int_1^{100} |\mathrm{TL}_a(x) - \mathrm{TL}_s(x)|\mathrm{d}x$ where subscripts a and s refer to the analytical and simulated transmission losses respectively. A grid convergence study is carried out, with discretizations ranging from just over four points per wavelength (ppw), corresponding to a Δx of 0.8 m, to 42 points per wavelength, i.e., $\Delta x = 0.08$ m. The computational domains cover the range $-150 \le x_1 \le 150$ and $x_2 \le 150$, and grid sizes range from around 10^5 grid points for the smallest mesh, to 10^7 points for the finest mesh. Figure 1 presents the results, with the transmission loss computed on the coarsest grid compared to the analytical solution in Fig. 1(a), and error as a function of discretization in Fig. 1(b). Characteristic interference lobes are observed in the transmission loss, and the computed solution with the coarsest discretization of only 4 ppw, despite significant attenuation, provides correct trends for these lobes, over the entire 100 m of the propagation domain. This distance corresponds to approximately 30 wavelengths, and thus the algorithm's capacity to propagate acoustics with relatively low discretizations over long distances is illustrated.

Figure 1(b) shows the convergence of the numerical solution toward the analytical one as the computational grid is refined. This study is carried out with a constant value of CFL = 0.5, which means the time step varies linearly with Δx. In order for the cumulative effect of the high-order low-pass filtering to be comparable for the different simulations, the low-pass filtering strength σ[27] is chosen to be inversely proportional to the time step. For example, dividing the grid step by two also halves the time step, and the filtering coefficient σ is therefore also halved. Mesh and simulation parameters for this study are provided in Table II. The variation of error ϵ with grid density is observed to be very close to third order, and thus the overall solver behavior here is of second order. This second-order behavior is due to the fact that for this relatively large CFL, time integration, performed with a second-order Runge-Kutta algorithm here, is the leading source of error. If a smaller CFL value were chosen, such

Redistribution subject to ASA license or copyright; see http://acousticalsociety.org/content/terms. Download to IP: 156.18.39.37 On: Fri, 07 Mar 2014 09:48:20

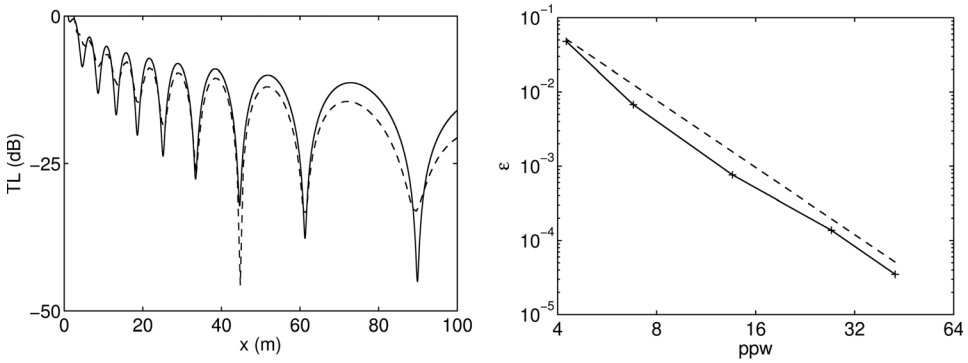

FIG. 1. (a) Transmission loss (TL) as a function of distance for a monopole above a rigid ground: — analytical solution, – – – – solution computed on $\Delta x = 0.8$ m grid, i.e., 4.25 ppw. (b) Computational error ϵ as a function of grid discretization in points per wavelength (ppw): –+ computed error, – – – – third order variation ($\epsilon \sim \text{ppw}^{-3}$).

that the leading error term were due to the spatial differencing, the finite difference scheme's order would dictate the variation of ϵ with grid density.

B. Acoustic source in an upwardly refracting atmosphere

A similar investigation is carried out for an atmosphere with a vertically stratified speed of sound, a condition typically found in a realistic atmosphere. Over long propagation distances, acoustic refraction due to a gradient in sound speed can result in the formation of wave guides or zones of silence, depending on the sign of the temperature gradient.[41] Over the relatively small distance considered in the previous homogeneous test case, and for a moderate celerity gradient, acoustic refraction will simply modify slightly the transmission loss profile, in particular changing the distance between consecutive TL extrema. This configuration should both test the reflection condition in more realistic conditions, and demonstrate that refraction effects are correctly captured by the numerical solution. For the present study, the temperature gradient is chosen negative in order to yield an upward refracting atmosphere as often found at ground level in long-range propagation problems.

As in the homogeneous case, a monopole at a frequency of 100 Hz is placed 20 m above a rigid ground. Ambient pressure is again set to 10^5 Pa, but the speed of sound is now a function of altitude x_2, and given by $c_0(x_2) = c_0/\sqrt{1 + 2x_2/r_0}$, sometimes referred to as an n^2-linear medium. Values of $c_0 = 340$ m/s and $r_0 = 338.5$ m are chosen to provide a roughly linear variation of celerity close to the ground, of $dc_0/dx_2 \simeq 1/\text{s}$. It can be noted that an analytical solution can be written if density variations are neglected, although it is rather more involved than for a homogeneous atmosphere. Developments for the axisymmetric case can be found in Chap. 9–5 of Pierce's book[42] and in Sec. 2.5.1 of *Computational Ocean Acoustics*.[43] In a gravitationally stratified atmosphere, density decreases exponentially with altitude, but with the parameters of the present study the analytical approximation is indistinguishable from the numerical solution obtained on the finest grid. The quality of the computational field is assessed by comparing the numerically obtained TL over a distance of 100 m to that obtained on the finest grid.

TABLE II. Grid and simulation parameters: Δx, time step Δt and filtering strength σ for homogeneous atmosphere test case grid convergence study.

Δx	0.08	0.125	0.25	0.5	0.8
Δt	1.18×10^{-4}	1.84×10^{-4}	3.68×10^{-4}	7.35×10^{-4}	0.0012
σ	0.064	0.1	0.2	0.4	0.64

Figure 2(a) provides a comparison of the reference transmission loss, computed on the finest grid with $\Delta x = 0.06$ m and that obtained on the coarsest mesh with $\Delta x = 0.8$ m. In Fig. 2(b), the effect of grid resolution on computational error ϵ is shown, for $4.25 \leq \text{ppw} \leq 42.5$ at ground level. It should be noted that due to the temperature profile, the acoustic wavelength, and therefore also the grid resolution, diminish with altitude. The numbers of points per wavelength are accordingly all given at ground level. As in the homogeneous case, even the coarsest grid resolution of 4.25 ppw provides a reasonable match to the analytical solution, and error ϵ is found to decrease again roughly with the third power of grid refinement. Comparing Figs. 1(b) and 2(b), it can be noted that for a given $k\Delta x$, error is slightly higher for the temperature-stratified case than for the homogeneous case. This can be attributed to the reduction in acoustic wavelength due to thermal stratification.

These two propagation test cases show that the solver is capable of accurate predictions of both acoustic amplitude and phase at long distances from a source, with grid discretizations greater than four points per wavelength. The solver is also shown to maintain its overall accuracy in the presence of slowly varying atmospheric inhomogeneities.

IV. SOURCE AMPLITUDE EFFECTS ON LONG DISTANCE PROPAGATION

The numerical algorithm described in the previous sections is used to perform an investigation of the effect of source amplitude on time signatures for long-distance infrasound propagation through a realistic atmosphere. After a presentation of the problem's atmospheric conditions and of the acoustic source, a brief description of the resulting acoustic signals at long range is given. Aspects relating to the results' accuracy are investigated, before discussing modifications to signals recorded at long range due to source amplitude.

A. Atmospheric configuration

The atmosphere used in this work is described below. Air is modeled as a perfect gas, with values of specific heat

Redistribution subject to ASA license or copyright; see http://acousticalsociety.org/content/terms. Download to IP: 156.18.39.37 On: Fri, 07 Mar 2014 09:48:20

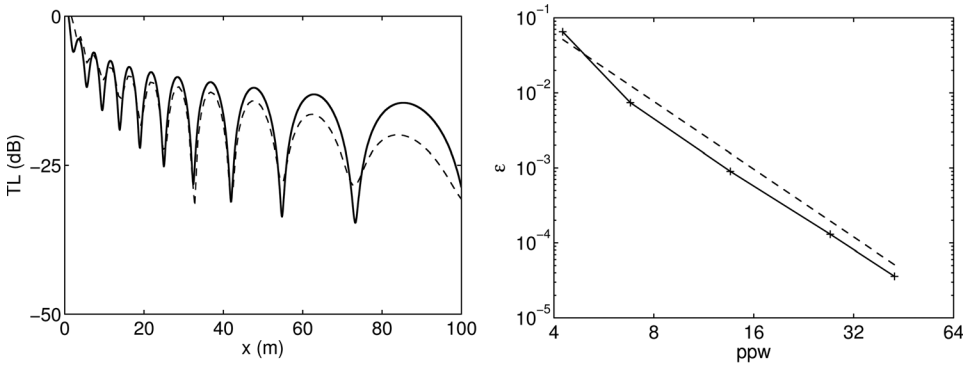

FIG. 2. (a) Transmission loss (TL) as a function of distance for a monopole above a rigid ground in a stratified atmosphere: — reference solution computed on $\Delta x = 0.06$ m grid, – – – – solution computed on $\Delta x = 0.8$ m grid. (b) Computational error ϵ as a function of grid discretization in points per wavelength (ppw) at ground level: –+ computed error, – – – – third order variation ($\epsilon \sim \text{ppw}^{-3}$).

ratio $\gamma = 1.4$ and molecular weight m_o independent of altitude. Values of important parameters are provided in Table III. The gravitational field is assumed of constant strength, with $g = 9.8$ m s^{-2}. A spline-based celerity profile which follows the main trends of a realistic atmosphere is used to determine ambient pressure and density as a function of altitude thanks to the hydrostatic equilibrium relation $d\bar{p}/dx_2 = -\bar{\rho}g = -g\bar{p}/RT$, and a pressure of 10^5 Pa at ground level. Spline knot locations and values are taken from,[44] with an additional knot location at 230 km altitude to allow a profile to be defined throughout the top sponge zone. The spline coefficients are listed in Table IV, and used as follows: for $x_2 \in [x_2^i, x_2^{i+1}]$, $\bar{c}(x_2) = ac^i + bc^{i+1} + 1/6\left[(a^3 - a)c''^i + (b^3 - b)c''^{i+1}\right](x_2^{i+1} - x_2^i)^2$, where $a = (x_2^{i+1} - x_2)/(x_2^{i+1} - x_2^i)$ and $b = 1 - a$.

The temperature profile, and the corresponding speed of sound, are shown in Fig. 3 along with the Väisälä-Brunt frequency, defined by $N = \text{sign}(N^2) \times |N^2|^{1/2}$, where $N^2 = -g/\bar{\rho}\, \mathrm{d}\bar{\rho}/\mathrm{d}x_2 - g^2/\bar{c}^2$. The profiles of temperature and celerity have two local minima, corresponding to the tropopause and mesopause acoustic waveguides located at altitudes of around 18 and 90 km, respectively. The atmospheric profile is statically stable, as indicated by the positive values of $N(x_2)$. All test cases in what follows are performed in an atmosphere at rest.

The sound source in the computations, implemented as a forcing term to the energy equation, has a Gaussian spatial envelope and a simple time variation given by

$$S(x_1, x_2, t) = \frac{1}{2}\mathcal{A}\sin(\omega_s t)\left[1 - \cos\left(\frac{\omega_s t}{2}\right)\right]\Pi \times \left(\frac{2}{T_s}\left(t - \frac{T_s}{4}\right)\right) e^{-\ln 2\left(x_1^2 + x_2^2\right)/b^2}, \quad (9)$$

with a frequency of $f_s = 1/T_s = 0.1$ Hz and a half-width of $b = 600$ m. In the previous equation, $\Pi(x)$ represents the standard box function. The parameter $\mathcal{A}$, expressed in J m^{-3}, is used to adjust source strength. It is placed at ground level at the origin of the domain, $(x_1, x_2) = (0, 0)$. The signal resulting from this source is illustrated in Fig. 4, which presents pressure fluctuations recorded at ground level at 1 km from the source, along with the corresponding energy spectral density. The physical part of the computational domain spans 600 km in the x direction and 160 km in the vertical direction. The reference grid has a spatial step of $\Delta x_1 = \Delta x_2 = 200$ m, and contains a total of 3.4×10^6 points. Additional details on grid resolution effects will be provided in Sec. IV C 2. A CFL value of 0.5 is used, which yields a time step of $\Delta t = 0.5\Delta x/\max(\bar{c}) = 0.17$ s based on the highest frozen speed of sound, found in the thermosphere. Time signals are recorded at ground level every 50 km, and compared as a function of source amplitude $\mathcal{A}$.

In the equations used for this work, no account is taken of atmospheric absorption due to molecular relaxation. Relaxation effects are expected to be strongest in the high atmosphere, i.e., where non-linear propagation effects are also maximal. Hence quantitative aspects described in this work are likely to be slightly different once relaxational effects are included.[24] The two-dimensional nature of this study also precludes a direct comparison of quantitative aspects of this work to actual ground-recorded signals. Indeed, geometrical amplitude attenuation in two dimensions is proportional to $1/\sqrt{r}$, where r is the propagation distance, while in three dimensions it is proportional to $1/r$. Different ground arrivals at a given location having propagated over different distances, this means that the relative amplitudes of acoustic phases in a 2D computation will not vary with distance as they would in three dimensions. As an additional consequence, non-linear effects, by essence amplitude-dependent, will not be quantitatively

TABLE III. Constant parameters for the atmospheric composition.

γ	c_p (J kg^{-1} K^{-1})	c_v (J kg^{-1} K^{-1})	R (J kg^{-1} K^{-1})	m_0 (kg mol^{-1})
1.4	1004.5	717.5	287	29×10^{-3}

TABLE IV. Spline coefficients for sound speed profile used to generate the stratified atmospheric profile.

x_2 (km)	$c(x_2)$	$c''(x_2)$
0	340	0
10	300	0.393009
20	290	0.227963
50	330	−0.272237
70	290	0.01924251
90	265	0.420267
120	425	−0.0970527
160	580	−0.194266
230	450	0

Redistribution subject to ASA license or copyright; see http://acousticalsociety.org/content/terms. Download to IP: 156.18.39.37 On: Fri, 07 Mar 2014 09:48:20

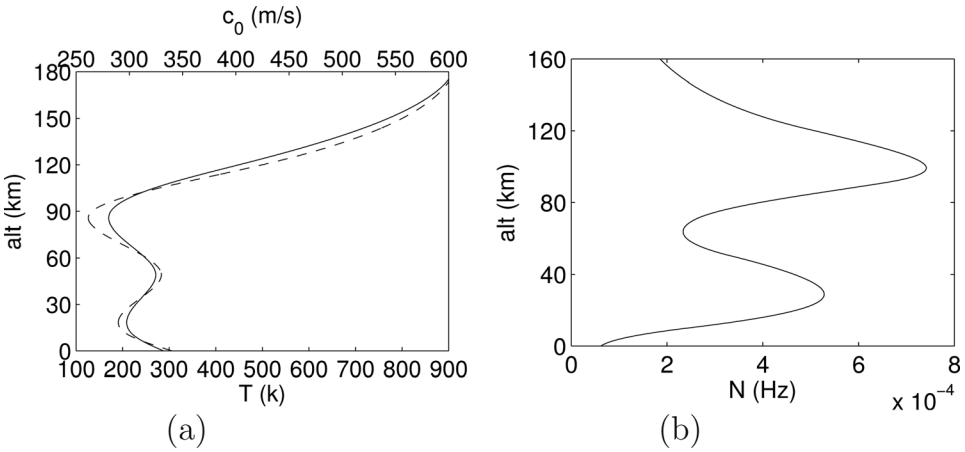

FIG. 3. (a) Profiles of temperature (—) and of speed of sound (– – – –), and (b) the Väisälä-Brunt frequency, as a function of altitude.

correctly predicted. These effects are overestimated in all cases since amplitude decreases more slowly in 2D than 3D, and the overestimation will also be stronger for high traveling phases. Nevertheless, the qualitative variations that will be described are expected to hold, and the computational approach followed in this work is readily applicable in 3D for future work.

B. Overview of results

Figure 5(a) shows a snapshot of the acoustic field normalized by the square root of mean density,[32] at $t = 1320$ s, which corresponds to the arrival time of the tropospheric phase *Iw* at the measurement location $x = 400$ km. The source amplitude in this case is $\mathcal{A} = 1\ \mathrm{J\ m^{-3}}$. Acoustic rays are superposed in gray. Three separate arrivals are identifiable in the acoustic field. The first wavefront to arrive is the tropospheric phase *Iw*, visible around $x_1 = 400$ km. It is not captured by rays emitted from the source location. The two subsequent arrivals have traveled higher through the atmosphere, both reaching the thermosphere. At distances larger than 330 km, the higher traveling It_b phase is seen to arrive before the lower It_a phase, due to its larger trace velocity. A strong caustic is clearly visible in the thermosphere at an altitude of 110 km between $x_1 = 180$ and $x_1 = 250$ km, and a second one can be seen at the end of the shadow zone, descending down from the thermosphere to reach ground level around $x_1 = 270$ km. The end of the shadow zone is also clearly visible in Fig. 5(b), where pressure signals recorded every 50 km along the ground are represented as a function of time and distance from the source. This time-distance plot highlights the lengthening of the pressure traces as distance from the source increases, due to the multiple arrivals. Also clearly visible is the difference in trace velocity between different phases, the higher traveling It_b phase having a substantially larger trace velocity than the other two. The brief description given above of the acoustic fluctuations illustrates well the fact that a simple initial source in a smooth atmospheric profile can yield a complex acoustic pattern downstream from the first shadow zone.

C. Numerical accuracy and large-amplitude signals

The overview of the acoustic field far from the source suggests that care should be taken in the correct treatment of non-linear wave steepening. Indeed, thermospheric arrivals, which are seen to account for a substantial part of the signals recorded downstream of the shadow zone, will have spent time during which the wave amplitude relative to ambient pressure is not small. In these conditions, significant non-linear waveform modification is expected. In this section, a brief assessment of the non-linear filtering procedure described in Sec. II is given, and grid discretization requirements are revisited in light of the signals' high frequency content.

1. Non-linear filtering for large-amplitude signals

The effect of the non-linear filtering technique described in Sec. II is examined on a simple configuration of

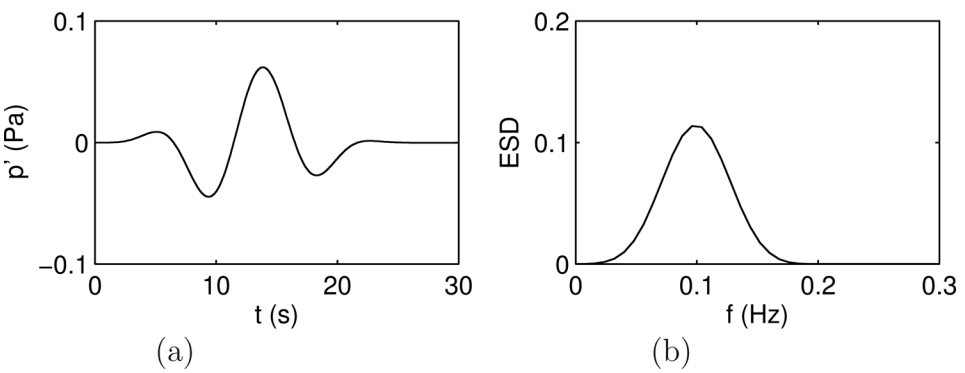

FIG. 4. Source characteristics. (a) fluctuating pressure signal at 1 km from the source for a source amplitude of $\mathcal{A} = 1\ \mathrm{J\ m^{-3}}$. (b) Energy spectral density (ESD) of the fluctuating pressure signal.

Redistribution subject to ASA license or copyright; see http://acousticalsociety.org/content/terms. Download to IP: 156.18.39.37 On: Fri, 07 Mar 2014 09:48:20

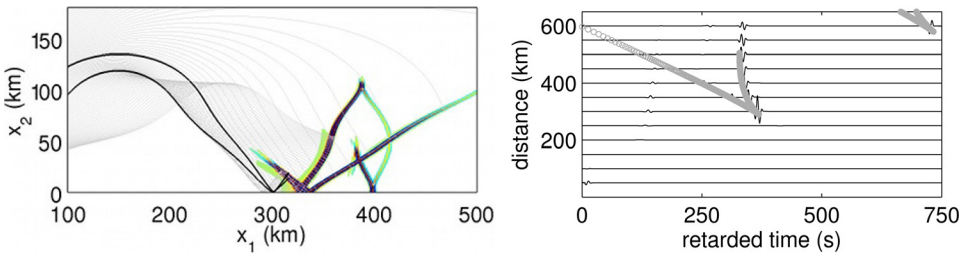

FIG. 5. (Color online) (a) View of pressure fluctuations p' normalized by $\sqrt{\bar{\rho}}$ at $t = 1320$ s for a source amplitude of $\mathcal{A} = 1$ J m^{-3}, with acoustic rays traced in gray; (b) pressure signals recorded at ground level as a function of retarded time and distance, for the same source amplitude: ○ arrivals predicted by ray-tracing, – – – – – $t - x_1/\bar{c}(x_2 = 0) = 0$.

atmospheric acoustic propagation, designed to induce non-linear effects which occur in long-range propagation phenomena.

This evaluation is carried out by studying the vertical propagation of a low-frequency high-amplitude acoustic signal in the atmospheric model described in Sec. IV A. The source model used is the same as that of the main study given by Eq. (9), with an amplitude of $\mathcal{A} = 1000$ J m^{-3}, located at ground level. The standard grid has a regular spacing of $\Delta_0 = 200$ m in both directions. Three computations are performed. The first is performed on the standard grid with no non-linear filtering, while the second is performed on the same grid but with the non-linear filtering applied with a filtering strength α, defined in Eq. (8), of $\alpha = 1$. The final computation, referred to as the reference computation, is performed on a finer grid ($\Delta' = \Delta_0/4$) and non-linear filtering is applied with a magnitude of $\alpha = 0.01$, to ensure numerical stability. Results from these three computations are compared at three different times in Figs. 6(a)–6(c).

These plots show vertical cuts of $p'/\sqrt{\bar{\rho}}$ as a function of altitude above the source, at $x_1 = 0$. In Fig. 6(a) taken at $t = 150$ s, first signs of wavefront steepening can be observed, due to the high source amplitude. There is no notable difference between the three sets of results, as the signal is still properly resolved by the numerical scheme on the coarse grid.

In Fig. 6(b), the solution obtained on the finer grid, represented by a solid black line, shows a well-defined central N-wave, preceded by a smaller partly formed leading N-wave. Weak Gibbs-type oscillations can be seen in the vicinity of the shocks, but their amplitude is a small fraction of the shock amplitudes. The coarse-grid solution obtained with the non-linear filtering (solid gray line) is in very good overall agreement with the reference solution. Gibbs oscillations are effectively removed. The peak amplitude of the shocks is slightly lower than that of the reference peaks and the shock fronts are slightly less steep, but this an unavoidable consequence of any filtering procedure. The coarse-grid unfiltered solution, shown by a gray dashed line, is similar to the reference solution in overall shape, but exhibits strong oscillations around it. These oscillations can be interpreted as strong Gibbs oscillations, which are not properly resolved by the numerical scheme and which therefore are not propagated at the correct velocity.

In the final Fig. 6(c) taken at 375 s, two well defined N-waves can be seen in the fine-grid signal, the leading lower amplitude wave having had time to become fully shocked. The coarse-grid solution obtained without non-linear filtering shows a reasonable overall match with the fine-grid signal, except in the vicinity of the leading shock fronts. Indeed, spurious peaks of amplitude greater than that of the reference signal are visible. The first of these peaks is notably ahead of the reference signal. This can be explained by noting the strong overshoots in Fig. 6(b) which will travel faster than the reference shock front. The analysis of such a signal obtained with no non-linear filtering would yield, among other problems, erroneous arrival times. The signal obtained with the filtering procedure does not exhibit this artifact, on the contrary matching the reference signal well.

In summary, a self-adjusting non-linear filtering methodology has been briefly tested for long-distance acoustic propagation computations with the Navier-Stokes equations. The non-linear filtering technique successfully removes Gibbs oscillations, which can be a numerical requirement for computations dealing with strong shocks, and as such can be regarded as *shock-capturing*. Moreover it enables the proper

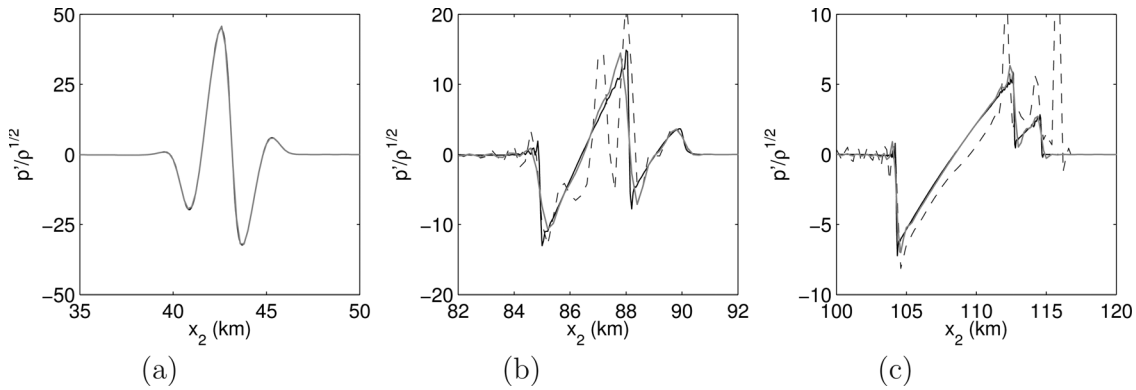

FIG. 6. Computed signals $p'/\sqrt{\bar{\rho}}(x_1 = 0, x_2)$ at (a) $t = 150$ s, (b) $t = 300$ s, and (c) $t = 375$ s: — computation on finer grid ($\Delta x/4$), —— computation with non-linear filtering and – – – – computation without non-linear filtering, both on standard grid.

Redistribution subject to ASA license or copyright; see http://acousticalsociety.org/content/terms. Download to IP: 156.18.39.37 On: Fri, 07 Mar 2014 09:48:20

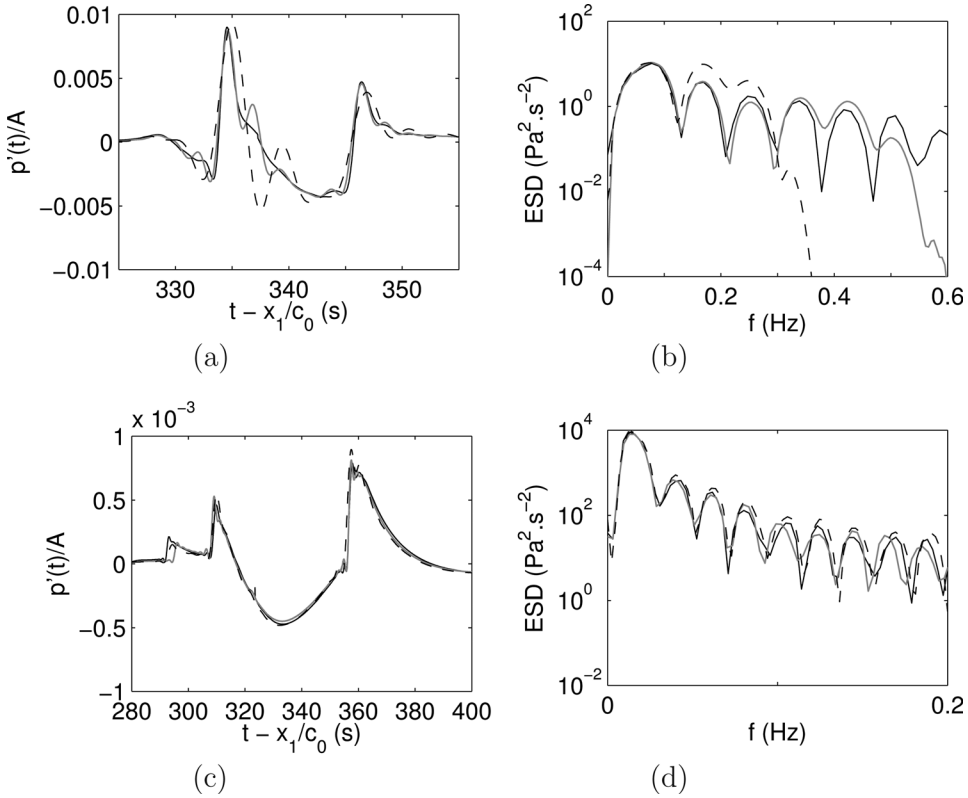

FIG. 7. Low thermospheric arrival recorded at $x_1 = 400$ km and $x_2 = 0$: (a) non-dimensional time signal and (b) ESD for $\mathcal{A} = 10^2$ J m^{-3}; (c) non-dimensional time signal and (d) ESD for $\mathcal{A} = 5 \times 10^3$ J m^{-3}. Solutions obtained using – – – – standard grid with Δ_0 spacing, —— $\Delta_0/2$ grid spacing, and — — — $\Delta_0/3$ grid spacing.

computation of shock-front velocities for relatively poorly discretized waves. This last point is essential if Navier-Stokes computations are to be used to study arrival times of acoustic signals over long propagation distances.

2. Grid resolution for realistic propagation

Strong non-linear effects will be highlighted in the results described in Sec. IV D. These non-linear variations change the spectral content of time signals, and therefore their spatial and time discretization. A larger error will naturally be committed on smaller wavelengths generated by non-linear processes than on the base wavelengths emitted by the source. A brief assessment of the impact of this is now provided, by comparing data obtained on the standard grid with $\Delta x_1 = \Delta x_2 = \Delta_0$ to results from a second grid with twice the spatial resolution and a third grid which is three times finer in both directions.

The source described in Sec. IV A having a principal frequency of 0.1 Hz, the standard grid spacing of 200 m yields a discretization of 17 points per wavelength at ground level and of 13 points per wavelength at an altitude of 90 km where the sound speed profile reaches its minimum.

These values may seem large when compared with those from the test cases presented in Sec. III, but they are necessary to allow the non-linear wave steepening described previously. The minimum discretization of 13 points per wavelength for the source's central frequency for example allows a reasonable representation of the second harmonic of this wavelength. For source strengths such that no non-linear signal modification is observed over the whole computational domain, i.e., for $\mathcal{A} < 1$ J m^{-3}, results from a computation performed on a grid which is twice as fine show negligible difference with those from the reference grid. As the source strength increases, differences appear, in particular in the high frequencies, as can be seen in Fig. 7 which traces the lower thermospheric arrival time signatures and energy spectral densities (ESD) for source amplitudes of $\mathcal{A} = 10^2$ and 5×10^3 J m^{-3} and for the three different grid resolutions, Δ_0, $\Delta_0/2$, and $\Delta_0/3$. This arrival is as expected the most sensitive to grid step size. For the lower amplitude source, the arrival is already strongly marked by non-linear effects, with a characteristic U-shape[45] resulting from an N wave having traversed a caustic. With the larger source amplitude, the period of the U-wave has increased from roughly 12 s to nearly 50 s, due to the increased non-linear lengthening in this case. This shift to lower frequencies is also clearly visible in the ESD shown in Figs. 7(b) and 7(d). For the source amplitude of 10^2 J m^{-3}, differences due to grid resolution are most visible in Fig. 7(a) between $t - x_1/\bar{c}(x_2 = 0) = 335$ and 345, where high-frequency oscillations are seen for the standard grid solution. These oscillations are far

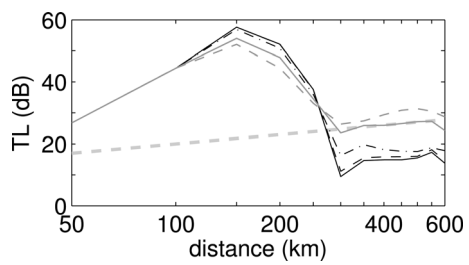

FIG. 8. Transmission loss at ground level as a function of distance from the source, for source amplitudes: — $\mathcal{A} = 1$, – – – – $\mathcal{A} = 10$, –·–·– $\mathcal{A} = 10^2$, —— $\mathcal{A} = 10^3$, — — — $\mathcal{A} = 5 \times 10^3$ J m^{-3}, and — — —: slope corresponding to 2D geometrical attenuation.

Redistribution subject to ASA license or copyright; see http://acousticalsociety.org/content/terms. Download to IP: 156.18.39.37 On: Fri, 07 Mar 2014 09:48:20

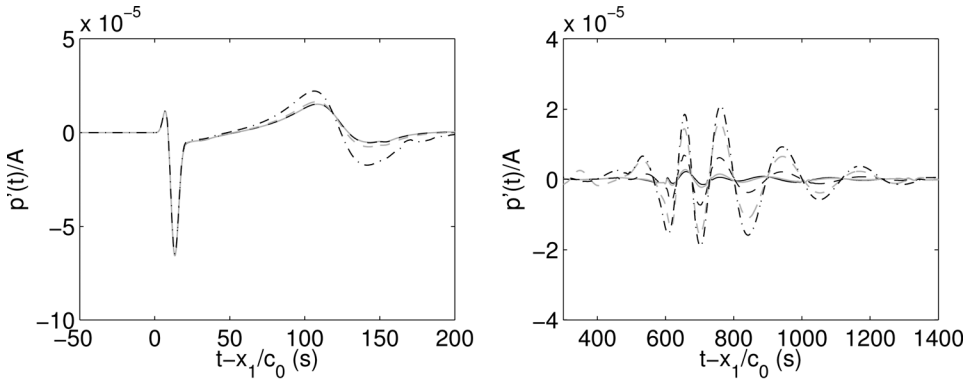

FIG. 9. Acoustic signals in the shadow zone; (a) first part of pressure signal at $x_1 = 150\,\text{km}$ and $x_2 = 0$, rendered non-dimensional by source strength $\mathcal{A}$. — $\mathcal{A} = 1$, —— $\mathcal{A} = 10$, – – – – $\mathcal{A} = 10^2$, — — — $\mathcal{A} = 10^3$, –·–·– $\mathcal{A} = 5 \times 10^3$ J m^{-3}; (b) late part of non-dimensional pressure signal at same location, same line styles as (a).

smaller on the second grid with twice the spatial resolution, and on the third grid they have almost disappeared. The oscillations are also visible in the ESD of this arrival shown in Fig. 7(b), where the first and second harmonics of the base frequency are clearly overestimated on the coarse grid, while the third and fourth harmonics are overestimated on the second grid. Despite these differences, the main features of the signal are well preserved on the standard grid, in particular the peak overpressure, the frequency shift due to shocked propagation, and the arrival time of this thermospheric phase. For the strongest source amplitude of 5×10^3 J m^{-3}, similar trends are observed in Figs. 7(c) and 7(d), the frequency shift and arrival times appearing to be correctly described by the standard grid. In fact, the standard grid seems to provide a better match for the strongest source level than for the weaker one. This can be explained by noting from Fig. 7(d) that the energy for this source level is concentrated at lower frequencies, and thus larger, better discretized, wavelengths. Overall, the standard grid used for the examination of source amplitude effects in this work appears sufficient to justify the trends to be described in Sec. IV D.

D. Effect of source strength

The aim of this study is to look at the effect of the source amplitude on the individual elements of the time signature. To this end, a parametric series of computations is performed for amplitudes ranging from $\mathcal{A} = 10^{-3}$ to 5×10^3 J m^{-3}, corresponding to pressure signals of approximately 4×10^{-4} to 2×10^3 Pa at 1 km from the source.

At a given distance from the source, the received signal amplitude is not simply proportional to the source amplitude, due to non-linear effects during propagation. This is illustrated in Fig. 8, which plots the TL at ground level, based on a reference distance of 1 km, $\text{TL}(x_1) = 10\log_{10}[E(x_1)/E(x_1 = 1\,\text{km})]$, where $E(x) = \int p'^2(x)dt$, for source amplitudes $\mathcal{A}$ of 1, 10, 10^2, 10^3, and 5×10^3 J m^{-3}. In the zone of silence, between 150 and 200 km, transmission loss is seen to decrease slightly as source strength is increased. Inversely, downstream of the zone of silence, for distances greater than 300 km, transmission loss increases with source strength. For source levels below 10^3 J m^{-3}, transmission loss in this zone is in fact lower than that given by geometrical spreading, represented as a thick dashed gray line in Fig. 8.

The behavior in the shadow zone is not predictable by commonly used techniques based on geometrical acoustics,[46] and is thus interesting to examine in more detail. Figure 9(a) shows the first 200 s of the pressure signal recorded at ground level 150 km from the source, scaled by source amplitude $\mathcal{A}$. The first arrival, starting just after $t - x_1/\bar{c}(x_2 = 0) = 0$ and thus corresponding to the tropospheric phase *Iw*, exhibits no effects of varying source strength. The second, however, arriving around $t - x_1/\bar{c}(x_2 = 0) = 100$, shows distinct non-linear variation for large source amplitudes. This arrival is due to the acoustic trapping in the tropospheric waveguide and diffraction off the top of the tropospheric waveguide, visible in Fig. 10(a) around $x_1 = 130$ km, $x_2 = 40$ km. Non-linear or self refraction is possibly also occurring due to the high acoustic intensity around the caustic. For source amplitudes below $\mathcal{A} = 10^2\,\text{J m}^{-3}$, the

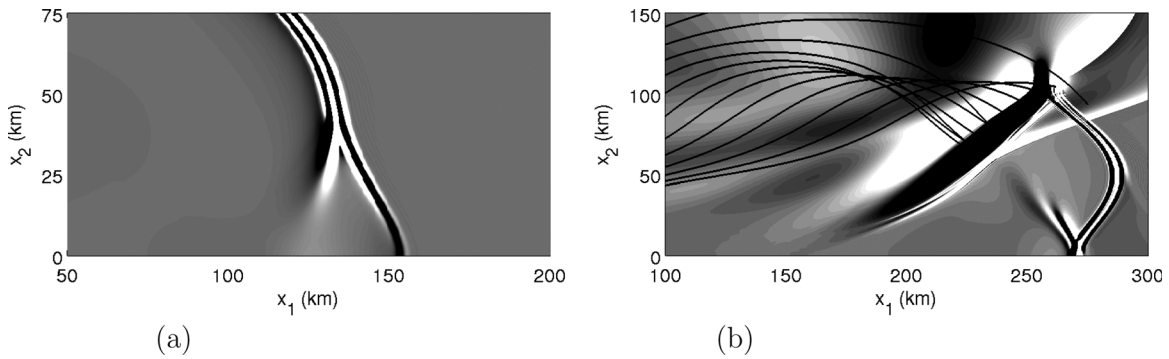

FIG. 10. Acoustic field in the shadow zone for a source amplitude of $\mathcal{A} = 10$ J m^{-3}; (a) structure of the pressure fluctuations $p'/\sqrt{\bar{\rho}}$ around the shadow zone at $t = 465$ s, (b) view of the same field at $t = 930$ s, with ray trajectories superimposed in black.

Redistribution subject to ASA license or copyright; see http://acousticalsociety.org/content/terms. Download to IP: 156.18.39.37 On: Fri, 07 Mar 2014 09:48:20

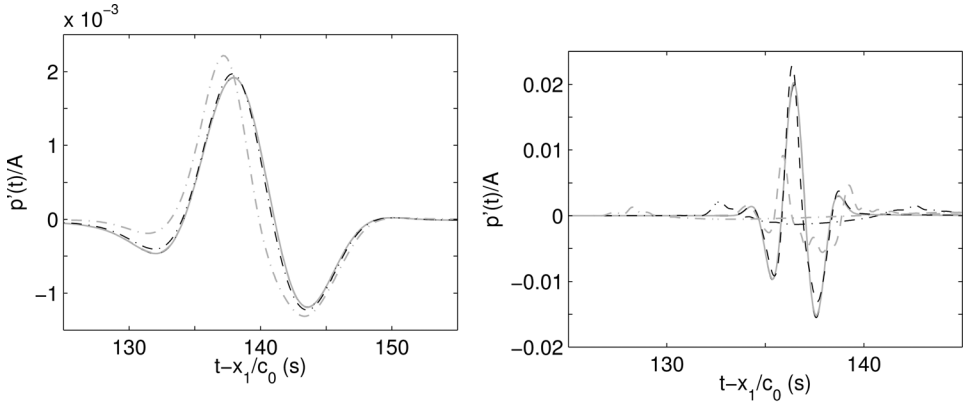

FIG. 11. Pressure signals recorded at $x_1 = 300$ km and $x_2 = 0$: (a) first arrival amplitude rendered non-dimensional by source strength, for — $\mathcal{A} = 10^{-2}$, – – – – $\mathcal{A} = 1$, –·–·– $\mathcal{A} = 10$, —— $\mathcal{A} = 10^2$, — — — $\mathcal{A} = 10^3$, —·—·— $\mathcal{A} = 5 \times 10^3$ J m^{-3}; (b) second arrival non dimensional amplitude at the same location, same line styles as (a).

waveform collapses almost perfectly to an antisymmetrical wavepacket of period roughly one sixth that of the source and of slightly lower amplitude than the direct arrival. For higher source levels, the waveform is amplified, reaching an amplitude larger than that of the direct arrival for $\mathcal{A} = 5 \times 10^3$ J m^{-3}. Finally, at 150 km from the source, a strong non-linear amplification in the pressure signal is observed for delays of between 400 and 1400 s after the direct arrival, as can be seen in Fig. 9(b). The strongest source yields a scaled pressure signal of more than 10 times the amplitude of that resulting from the weakest source. The origin of this part of the signal is highlighted in Fig. 10(b), which represents the scaled fluctuating pressure field during the late arrival. It comes from the thermospheric arrival, which, according to ray tracing does not touch ground before $x_1 = 280$ km, whose wavefront diffracts downward into the shadow zone. It is this diffraction phenomenon which appears to be dependent on the amplitude of the acoustic signal.

For the sound speed profile specified in this study, the geometrical zone of silence ends at $x_1 = 280$ km. Downstream of this point, transmission loss increases with increasing source amplitude, as previously noted from Fig. 8. Time signals recorded at a distance of 300 km from the source are compared in Fig. 11 for values of $\mathcal{A}$ ranging from 10^{-2} to 5×10^3 J m^{-3}, to identify the causes of the TL increase. These signals have two distinct contributions, one from the stratospheric eigenray, and a second from the thermospheric eigenray. The stratospheric contribution, shown in Fig. 11(a), the first to arrive at 300 km from the source, is relatively independent of source amplitude, up to $\mathcal{A} = 10^2$ J m^{-3}. As can be seen from Fig. 11(a), it arrives with a delay of approximately 130 s compared to a signal propagating along the ground, corresponding to an effective propagation speed of 296 m/s which is very close to the minimum speed in the tropospheric waveguide. The thermospheric contribution, shown in Fig. 11(b), is more sensitive to source amplitude, because it has traveled at a higher altitude and hence the ratio $p'/\bar{p}$ has reached larger values. Non-linear effects are visible for source amplitudes $\mathcal{A} \geq 1$. A very large reduction in amplitude is observed as source strength is increased, with a signal 20 times less intense for $\mathcal{A} = 5 \times 10^3$ than for $\mathcal{A} \leq 1$ J m^{-3}. The signal lengthening due to shock formation is better illustrated in Fig. 12 in which pressure signals are scaled by the maximum amplitude of their thermospheric arrivals. A U-shape typical of an N-wave having traversed a caustic[47] is observed for source amplitudes larger than $\mathcal{A} = 1$ J m^{-3}, and the stronger the source, the more stretched the U-shape, indicating shock formation occurring increasingly early along the propagation path. The arrival time of the peak overpressure for the largest amplitude source signal is brought forward by 42 s compared to the arrival times for very low source amplitudes. The significantly shortened travel time is due to the high travel path of the thermospheric rays. Indeed, although the overpressure ratio $p'/\bar{p}$ observed at ground level for the thermospheric arrivals is small, only 10^{-4} for the strongest source, this ratio is altitude-dependent during propagation,

$$\frac{p'}{\bar{p}} = \frac{p'}{\sqrt{\bar{\rho}}} \times \frac{\sqrt{\bar{\rho}}}{\bar{p}} = \frac{p'}{\sqrt{\bar{\rho}}} \times \sqrt{\frac{\gamma}{\bar{c}^2 \bar{p}}}$$

increasingly roughly exponentially with altitude. Assuming lossless propagation for simplicity and integrating backward along the ray trajectories, the overpressure ratio reaches a value of around one for the low thermospheric eigenray. This overpressure in turn induces significantly faster propagation, the shock wave traveling at a speed of $v_{\text{shock}} = \bar{c}[1 + (\gamma + 1)/(2\gamma)\, p'/\bar{p}]^{1/2}$ for a perfect gas.[48] This simplistic estimation suggests that shock formation occurred as the ray was climbing toward the thermosphere before reaching

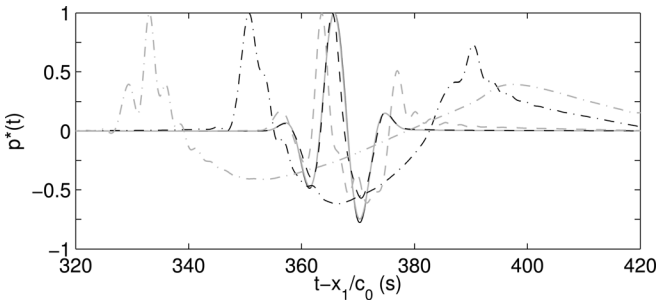

FIG. 12. Thermospheric arrivals of the pressure signals recorded at $x_1 = 300$ km and $x_2 = 0$, scaled by the maximum amplitude p^* of these arrivals, for — $\mathcal{A} = 10^{-2}$, – – – – $\mathcal{A} = 1$, –·–·– $\mathcal{A} = 10$, —— $\mathcal{A} = 10^2$, — — — $\mathcal{A} = 10^3$, —·—·— $\mathcal{A} = 5 \times 10^3$ J m^{-3}.

Redistribution subject to ASA license or copyright; see http://acousticalsociety.org/content/terms. Download to IP: 156.18.39.37 On: Fri, 07 Mar 2014 09:48:20

the caustic, which corresponds well with direct results from the simulation placing shock formation for this eigenray around $x_1 = 80$ km and $x_2 = 70$ km.

V. CONCLUSIONS

A computational approach for the study of long-range atmospheric infrasound propagation, based on the resolution of the full 2D Navier-Stokes equations with high-order space and time methods, is presented. This approach is used to examine the effect of source strength on pressure signals recorded at varying distance from the source. Time signatures recorded a long distance away from an acoustic source are shown to vary in a highly non-linear fashion as a function of source amplitude. For very low source amplitudes, time signatures collapse cleanly. For higher source amplitudes, the relative level of arrivals due to the different eigenrays is highly modified. Arrival times also vary strongly, with arrivals occurring earlier for higher traveling rays. Signals recorded in the shadow zone are also observed to undergo large modifications due to non-linearities. These non-linear waveform variations should be taken into account when attempting acoustic tomography of the atmosphere.

ACKNOWLEDGMENTS

This work was undertaken as part of a collaboration with the DASE department of the CEA/DAM/DIF. The authors would like to thank Dr. Blanc-Benon, Dr. Sturm, and Dr. Gainville for stimulating discussions. This work was performed within the framework of the Labex CeLyA of Université de Lyon, operated by the French National Research Agency (ANR-10-LABX-0060/ANR-11-IDEX-0007).

[1]M. E. Delany, "Sound propagation in the atmosphere-a historical review," Acustica **38**, 201–223 (1977).
[2]U. Ingård, "A review of the influence of meteorological conditions on sound propagation," J. Acoust. Soc. Am. **25**, 405–411 (1953).
[3]L. Sutherland and G. Daigle, "Atmospheric sound propagation," *Handbook of Acoustics* (Wiley, New York, 1998), pp. 305–329.
[4]K. Attenborough, "Sound propagation close to the ground," Ann. Rev. Fluid Mech. **34**(1), 51–82 (2002).
[5]C. de Groot-Hedlin, M. Hedlin, and D. Drob, "Atmospheric variability and infrasound monitoring," in *Infrasound Monitoring for Atmospheric Studies* (Springer, Dordrecht, 2009), pp. 475–507.
[6]M. West, R. A. Sack, and F. Walkden, "The fast field program (FFP). A second tutorial: Application to long range sound propagation in the atmosphere," Appl. Acoust. **33**(3), 199–228 (1991).
[7]M. West, K. Gilbert, and R. A. Sack, "A tutorial on the parabolic equation (PE) model used for long range sound propagation in the atmosphere," Appl. Acoust. **37**(1), 31–49 (1992).
[8]E. Salomons, *Computational Atmospheric Acoustics* (Kluwer Academic, Dordrecht, 2001), Chap. 4.
[9]M. V. Averyanov, V. A. Khokhlova, O. A. Sapozhnikov, Ph. Blanc–Benon, and R. O. Cleveland, "Parabolic equation for nonlinear acoustic wave propagation in inhomogeneous moving media," Acoust. Phys. **52**(6), 623–632 (2006).
[10]D. I. Blokhintsev, "Acoustics of a nonhomogeneous moving medium," Tech. Memorandum No. 1399, National Advisory Committee on Aeronautics (1956).
[11]A. D. Pierce, "Geometrical acoustics' theory of waves from a point source in a temperature- and wind-stratified atmosphere," J. Acoust. Soc. Am. **39**(6), 1261–1261 (1966).
[12]O. Gainville, Ph. Blanc-Benon, and J. Scott, "Infrasound propagation in realistic atmosphere using nonlinear ray theory," AIP Conf. Proc. **1474**(1), 343–346 (2012).
[13]C. I. Chessell, "Observations of the effects of atmospheric turbulence on low-frequency sound propagation," J. Acoust. Soc. Am. **60**(1), 29–33 (1976).
[14]O. Gainville, Ph. Blanc-Benon, E. Blanc, R. Roche, C. Millet, F. Le Piver, B. Despres, and P. F. Piserchia, "Misty picture: a unique experiment for the interpretation of the infrasound propagation from large explosive sources," in *Infrasound Monitoring for Atmospheric Studies* (Springer, Dordrecht, 2009), pp. 575–598.
[15]O. Marsden, L. Vayno, C. Bogey, and C. Bailly, "Study of long-range infrasound propagation with high-performance numerical schemes applied to the Euler equations," *Proceedings of the 13th Long Range Sound Propagation symposium*, *Lyon*, France, pp. 201–216 (2008).
[16]C. de Groot-Hedlin, "Finite-difference time-domain synthesis of infrasound propagation through an absorbing atmosphere," J. Acoust. Soc. Am. **124**(3), 1430–1441 (2008).
[17]C. de Groot-Hedlin, "Nonlinear synthesis of infrasound propagation through an inhomogeneous, absorbing atmosphere," J. Acoust. Soc. Am. **132**(2), 646–656 (2012).
[18]V. Ostashev, K. Wilson, L. Liu, D. Aldridge, N. Symons, and D. Marlin, "Equations for finite-difference, time-domain simulation of sound propagation in moving inhomogeneous media and numerical implementation," J. Acoust. Soc. Am. **117**(2), 503–517 (2005).
[19]S. Del Pino, B. Després, P. Havé, H. Jourdren, and P. F. Piserchia, "3D finite volume simulation of acoustic waves in the earth atmosphere," Comput. Fluids **38**, 765–777 (2009).
[20]D. Dragna, B. Cotté, Ph. Blanc-Benon, and F. Poisson, "Time-domain simulations of outdoor sound propagation with suitable impedance boundary conditions," AIAA J. **49**(7), 1420–1428 (2011).
[21]W. Hoffmann, R. Kebeasy, and P. Firbas, "Introduction to the verification regime of the comprehensive nuclear-test-ban treaty," Phys. Earth Planet Inter. **113**(1), 5–9 (1999).
[22]A. Le Pichon, E. Blanc, and A. Hauchecorne, "Contribution of infrasound monitoring for atmospheric remote sensing," in *Infrasound Monitoring for Atmospheric Studies* (Springer, Dordrecht, 2009), pp. 629–646.
[23]L. C. Sutherland and H. E. Bass, "Atmospheric absorption in the atmosphere up to 160 km," J. Acoust. Soc. Am. **115**(3), 1012–1032 (2004). See also Erratum: J. Acoust. Soc. Am. **120**(5), 2985 (2006).
[24]G. Hanique-Cockenpot, *Etude numérique de la propagation non linéaire des infrasons dans l'atmosphere* (Numerical study of non-linear infrasound propagation in atmosphere), Ph.D. thesis, Ecole Centrale de Lyon, 2011.
[25]J. Lighthill, *Waves in Fluids* (Cambridge University Press, Cambridge, 1974), Chap. 4.
[26]C. Bogey and C. Bailly, "A family of low dispersive and low dissipative explicit schemes for noise computations," J. Comput. Phys. **194**(1), 194–214 (2004).
[27]J. Berland, C. Bogey, O. Marsden, and C. Bailly, "High-order, low dispersive and low dissipative explicit schemes for multiple-scale and boundary problems," J. Comput. Phys. **224**, 637–662 (2007).
[28]C. Bogey, N. De Cacqueray, and C. Bailly, "A shock-capturing methodology based on adaptive spatial filtering for high-order non-linear computations," J. Comput. Phys. **228** 1447–1465 (2009).
[29]D. Gaitonde and M. Visbal, "Padé-type higher-order boundary filters for the Navier-Stokes equations," AIAA J. **38**(11), 2103–2112 (2000).
[30]C. K. W. Tam and J. C. Webb, "Dispersion-relation-preserving finite difference schemes for computational acoustics," J. Comput. Phys. **107**, 262–281 (1993).
[31]D. J. Bodony, "Analysis of sponge zones for computational fluid mechanics," J. Comput. Phys. **212**(2), 681–702 (2006).
[32]P. G. Bergmann, "The wave equation in a medium with a variable index of refraction," J. Acoust. Soc. Am. **17**(4), 329–333 (1946).
[33]S. Pirozzoli, "On the spectral properties of shock-capturing schemes," J. Comput. Phys. **219**(2), 489–497 (2006).
[34]O. Marsden, C. Bogey, and C. Bailly, "High-order curvilinear simulations of flows around non-Cartesian bodies," J. Comput. Acoust. **13**(4), 731–748 (2005).
[35]O. Marsden, X. Gloerfelt, and C. Bailly, "Direct noise computation of adaptive control applied to a cavity flow," C. R. Acad. Sci. **331**, 423–429 (2003).
[36]O. Marsden, C. Bogey, and C. Bailly, "Direct noise computation of the turbulent flow around a zero-incidence airfoil," AIAA J. **46**(4), 874–883 (2008).

Redistribution subject to ASA license or copyright; see http://acousticalsociety.org/content/terms. Download to IP: 156.18.39.37 On: Fri, 07 Mar 2014 09:48:20

[37]C. Bogey, O. Marsden, and C. Bailly, "Large-eddy simulation of the flow and acoustic fields of a Reynolds number 10^5 subsonic jet with tripped exit boundary layers," Phys. Fluids **23**(3), 035104 (2011).
[38]O. Marsden, C. Bogey, and C. Bailly, "Investigation of flow features around shallow round cavities subject to subsonic grazing flow," Phys. Fluids **24**(12), 125107 (2012).
[39]P. M. Morse and K. U. Ingard, *Theoretical Acoustics* (Princeton University Press, Princeton, 1987), Chap. 7.4.
[40]K. Wilson and L. Liu, "Finite-difference, time-domain simulation of sound propagation in a dynamic atmosphere," Tech. report ERDC/CRREL TR-04-12, Cold Regions Research and Engineering Lab, Hanover, NH (2004).
[41]K. Attenborough, S. Taherzadeh, H. E. Bass, X. Di, R. Raspet, G. R. Becker, A. Güdesen, A. Chrestman, G. A. Daigle, A. LEspérance, Y. Gabillet, K. E. Gilbert, Y. L. Li, M. J. White, P. Naz, J. M. Noble, and H. A. J. M. van Hoof, "Benchmark cases for outdoor sound propagation models," J. Acoust. Soc. Am. **97**(1), 173–191 (1995).
[42]A. D. Pierce, *Acoustics, An Introduction to Its Physical Principles and Applications*, 3rd ed. (Acoustical Society of America, Melville, NY, 1994), Chap. 9.5.
[43]F. B. Jensen, W. Kuperman, M. Porter, and H. Schmidt, *Computational Ocean Acoustics* (Springer, Dordrecht, 2011), Sec. 2.5.1.
[44]O. Marsden and O. Gainville "Nonlinear effects in infrasound propagation simulations," *Acoustics 2012 Nantes Conference* (2012).
[45]R. Marchiano, F. Coulouvrat, and R. Grenon, "Numerical simulation of shock wave focusing at fold caustics, with application to sonic boom," J. Acoust. Soc. Am. **114**(4), 1758–1771 (2003).
[46]C. de Groot-Hedlin, M. Hedlin, K. Walker, D. Drob, and M. Zumberge, "Evaluation of infrasound signals from the shuttle Atlantis using a large seismic network," J. Acoust. Soc. Am. **124**(3), 1442–1451 (2008).
[47]R. R. Rosales and E. G. Tabak, "Caustics of weak shock waves," Phys. Fluids **10**(1), 206–222 (1998).
[48]J. DuMond, E. Richard Cohen, W. K. H. Panofsky, and E. Deeds, "A determination of the wave forms and laws of propagation and dissipation of ballistic shock waves," J. Acoust. Soc. Am. **18**(1), 97–118 (1946).

Redistribution subject to ASA license or copyright; see http://acousticalsociety.org/content/terms. Download to IP: 156.18.39.37 On: Fri, 07 Mar 2014 09:48:20